Science Advances
AAAS

Supplementary Materials for

Discovering the gene-brain-behavior link in autism via generative machine learning

Shinjini Kundu *et al.*

Corresponding author: Shinjini Kundu, skundu2@jhmi.edu

Sci. Adv. **10**, eadl5307 (2024)
DOI: 10.1126/sciadv.adl5307

This PDF file includes:

Supplementary Text
Figs. S1 to S15
Tables S1 to S9
References

S1. No relationship between brain parenchymal volume and brain tissue distribution

The potential influence of brain parenchymal volume on brain tissue distribution was assessed by performing a linear regression analysis in the transport domain. When correcting for covariates of age, gender, gene cohort, and full-scale IQ, there was no statistically significant relationship between brain parenchymal volume and brain tissue distribution for either gray matter (Pearson correlation coefficient 0.12, p = 0.20) or white matter (Pearson correlation coefficient 0.21, p = 0.29). The scatter plots in Figure S1 illustrate the regression relationship between brain parenchymal volume and brain tissue distribution. Therefore, the variations in brain tissue distribution assessed in this paper are not accounted for by brain parenchymal volume differences.

a.

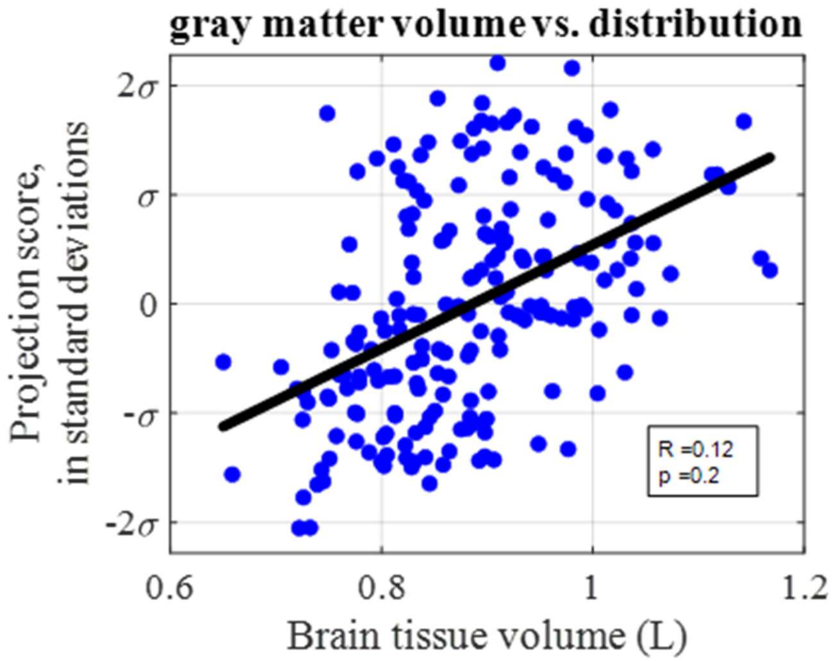

b.

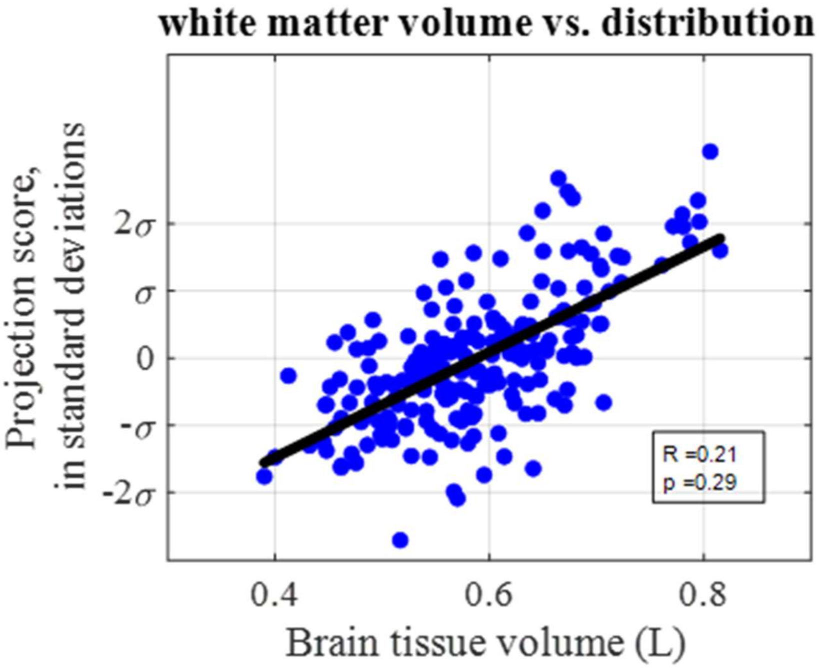

Figure S1. The relationship between total brain parenchymal volume and brain tissue distribution is not statistically significant for either (a) gray matter or (b) white matter when correcting for covariates of age, total full-scale IQ, gender, and gene cohort. Each point represents an individual subject when projected onto the direction in transport space that is maximally correlated with total brain parenchymal volume. FSIQ was missing for one subject.

S2. Gray matter variation not completely explained by white matter variation

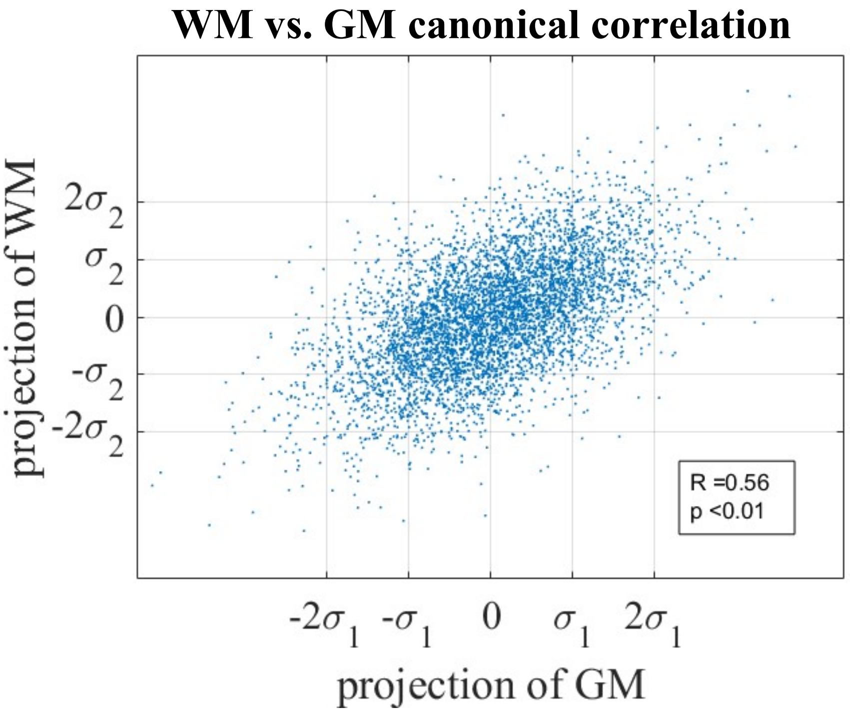

Figure S2. Data projected onto the top CCA direction from 100 iterations from the test set. Although the relationship between gray matter and white matter tissue distribution is statistically significant, the variance explained on unseen data is 31%.

The dependence between gray matter and white matter tissue distribution was measured using canonical correlation analysis (CCA) [66] in the transport domain. Figure S2 illustrates the correlation between gray matter and white matter tissue distribution when projected onto the top canonical direction. The CCA technique was iterated 100 times, with 75% of the dataset randomly sampled for training and the remaining 25% for testing in each iteration. The mean correlation coefficient in the test set is reported. Statistical significance of the computed direction was determined using permutation testing over T = 100 iterations.

We observe that the relationship between gray and white matter distribution is statistically significant (Pearson correlation coefficient 0.56, $p < 0.01$), with variance explained on unseen data of 31%. Therefore, their structural variations cannot be mutually explained fully, motivating separate analyses on gray and white matter.

S3. Classification using separate white matter and gray matter parenchymal volumes

The ability to distinguish CNV based on white and gray matter parenchymal volumes was evaluated, as illustrated in Figure S3. There is generally a positive correlation between gray matter and white matter volumes. Furthermore, duplication carriers typically have lower volumes compared to controls, while deletion carriers have the highest volumes. However, the distributions across CNV cohorts are overlapping, which limits the ability to discriminate CNV based solely on parenchymal volume.

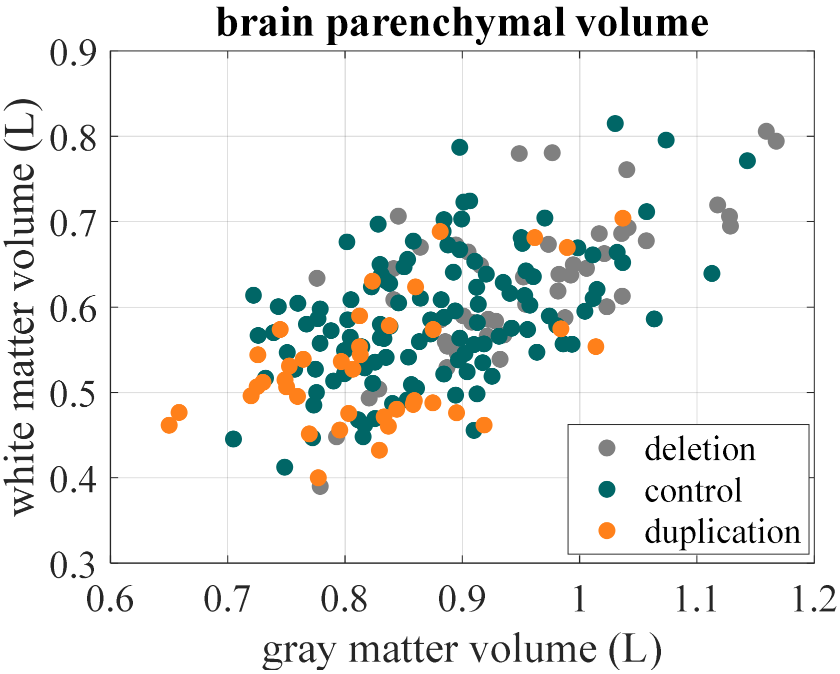

Figure S3. Parenchymal volumes, white matter vs. gray matter. Parenchymal volumes alone are insufficient to distinguish individuals with 16p11.2 copy number variations.

A penalized linear discriminant analysis (pLDA) classifier was trained using original white matter and gray matter parenchymal volumes as separate dimensions. Table S1 summarizes the classification accuracy achieved through stratified repeated 10-fold cross validation, using the same folds as detailed in the main text. The classification is not much better than chance (Cohen's kappa 0.19). However, it is important to consider multicollinearity when using both gray and white matter together as features in the model.

The discriminant ability of age, gender, and separate gray matter and white matter volumes was assessed to enable direct comparison with Table 3 in the main text. A pLDA classifier was trained and tested using stratified repeated 10-fold cross validation with the same folds as in the main text. The results in Table S1 show that CNV discrimination is not much better than chance (Cohen's kappa 0.19 to 0.23). White matter volume appears to enable better CNV discrimination than gray matter.

Overall, the results indicate that the ability to discriminate 16p11.2 CNV is driven by tissue changes in white and gray matter not captured by volume alone.

Table S1. Separating gray and white matter parenchymal volume

Features	**Test accuracy**	**Sensitivity *(deletion/control/ duplication)***	**Specificity *(deletion/control/ duplication)***	**Cohen's kappa**
White and gray matter volumes only	43.8 [40.7, 46.8]%	57.4 [54.4, 60.5]% / 27.9 [25.1, 30.7]% / 74.1 [71.4, 76.8]%	71.3 [68.4, 74.1]% / 77.5 [74.9, 80.1]% / 69.5 [66.7, 72.4]%	0.19 [0.17, 0.21]
Age, gender, and white matter volume	46.6 [43.6, 49.7]%	61.7 [58.7, 64.7]% / 31.5 [28.6, 34.3]% / 73.4 [70.6, 76.1]%	71.9 [69.1, 74.7]% / 80.0 [77.5, 82.5]% / 71.1 [68.3, 73.9]%	0.23 [0.20, 0.25]
Age, gender, and gray matter volume	43.6 [40.5, 46.7]%	61.6 [58.6, 64.6]% / 28.4 [25.6, 31.2]% / 66.8 [63.9, 69.7]%	74.0 [71.2, 76.7]% / 79.9 [77.4, 82.4]% / 65.4 [62.5, 68.4]%	0.19 [0.17, 0.22]

S4. Visualization of 3D TBM-generated brain structural variations

The discriminant subspaces in Figure 3a-d in the main manuscript can be interrogated at different points along direction 1 and direction 2 and the corresponding brain structural variations defining each class boundary can be directly visualized through inverse 3D TBM transformation. This approach allows us to visualize the variations in brain morphology enabling sensitive discrimination of 16p11.2 genetic cohorts. Figure S4 and S5 correspond to the computer-generated images for white matter and gray matter, respectively, when the discriminant subspaces in Figure 3a,c and Figure 3b,d are sampled in the main manuscript.

Figure S4 shows the discriminant subspace for white matter tissue computed in the transport domain. The discriminant subspace for gray matter is shown in Figure S5.

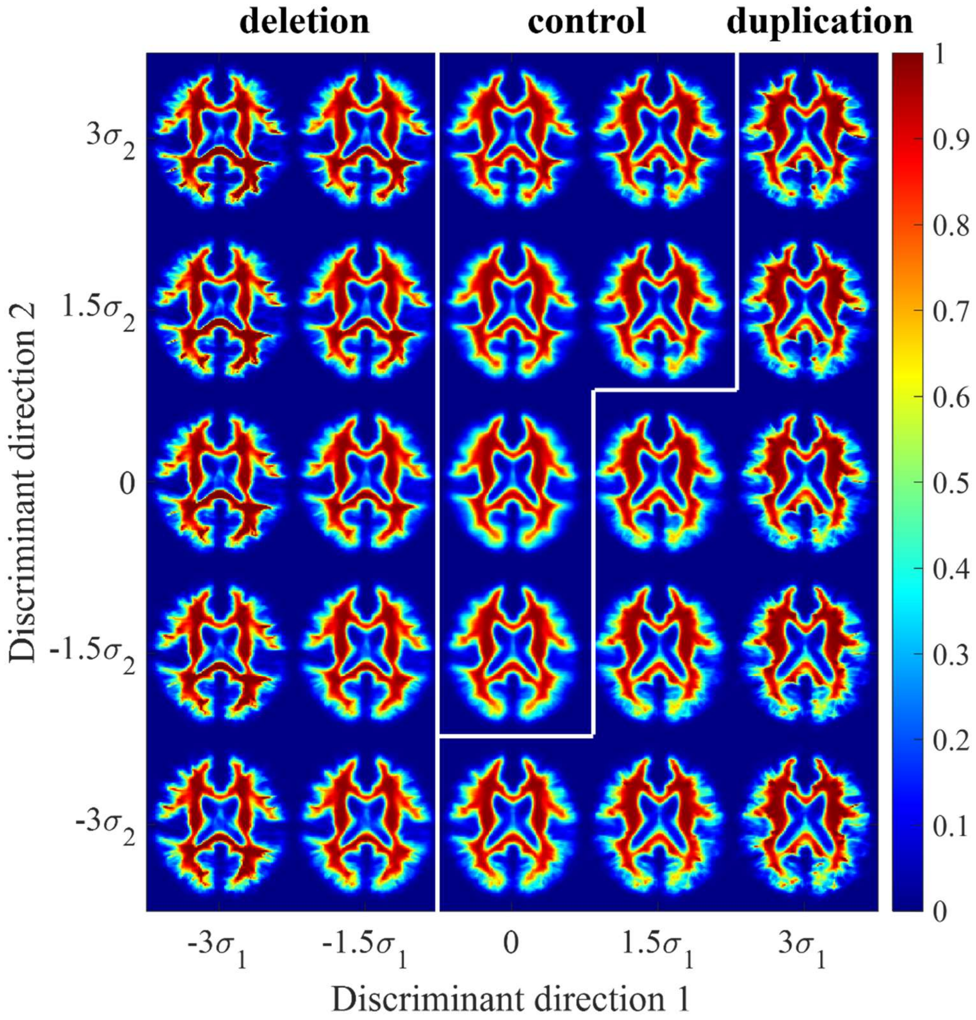

Figure S4. Brain images generated by 3D TBM when sampling the discriminant subspace in Figure 3a,c. Here, 0 represents the mean image, and σ_1 and σ_2 represent standard deviations from the mean in direction 1 and direction 2 respectively. Color represents tissue density.

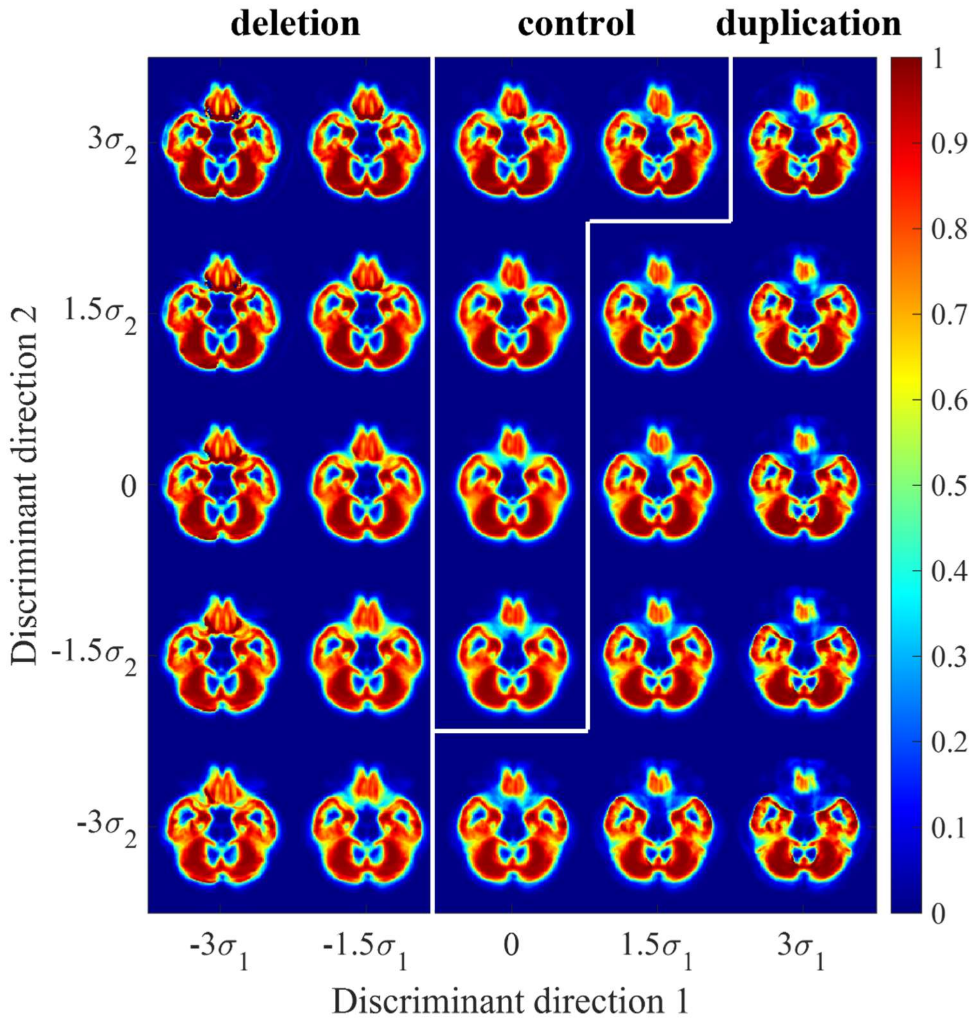

Figure S5. Brain images generated by 3D TBM when sampling the discriminant subspace in Figure 3b,d. Here, 0 represents the mean image, and σ_1 and σ_2 represent standard deviations from the mean in direction 1 and direction 2 respectively. Color represents tissue density.

Example visual differences are illustrated in TBM-generated Figures S6 and S7, which are sampled along discriminant direction 1. In slice 85, we see a characteristic increase in white matter density in the superior cerebral (frontoparietal) white matter (deletion carriers > controls > duplication carriers). Slices 73 and 63 show changes in occipital white matter density, including the splenium of the corpus callosum (deletion carriers > controls > duplication carriers). Slice 53 shows differences in the inferior temporal (duplication carriers > controls > deletion carriers) and inferior frontal (deletion carriers > controls > duplication carriers) regions, while the brainstem is unchanged. In slice 47, the superior vermis of the cerebellum is affected (deletion carriers > controls > duplication carriers). Finally, in slice 39, we see that the cerebellar hemispheric white matter is affected such that (deletion carriers > controls > duplication carriers).

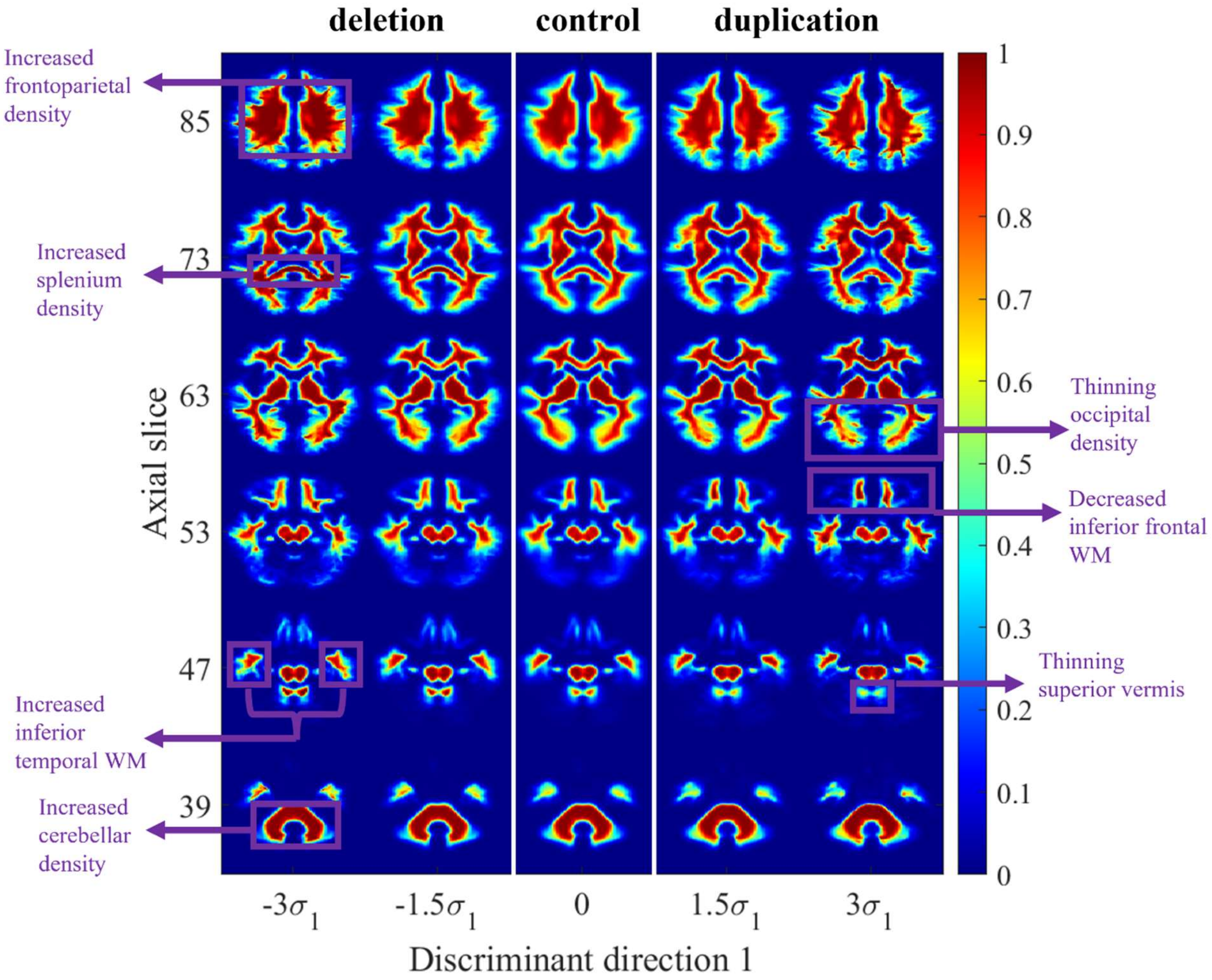

Figure S6. White matter. These computer-generated images can be interpreted to understand the differences that enable high classification accuracy by visualizing along discriminant direction 1. Color represents tissue density. Here, σ_1 is the standard deviation from the mean (represented by score 0). The axial slices best showing the changes in white matter morphology are shown.

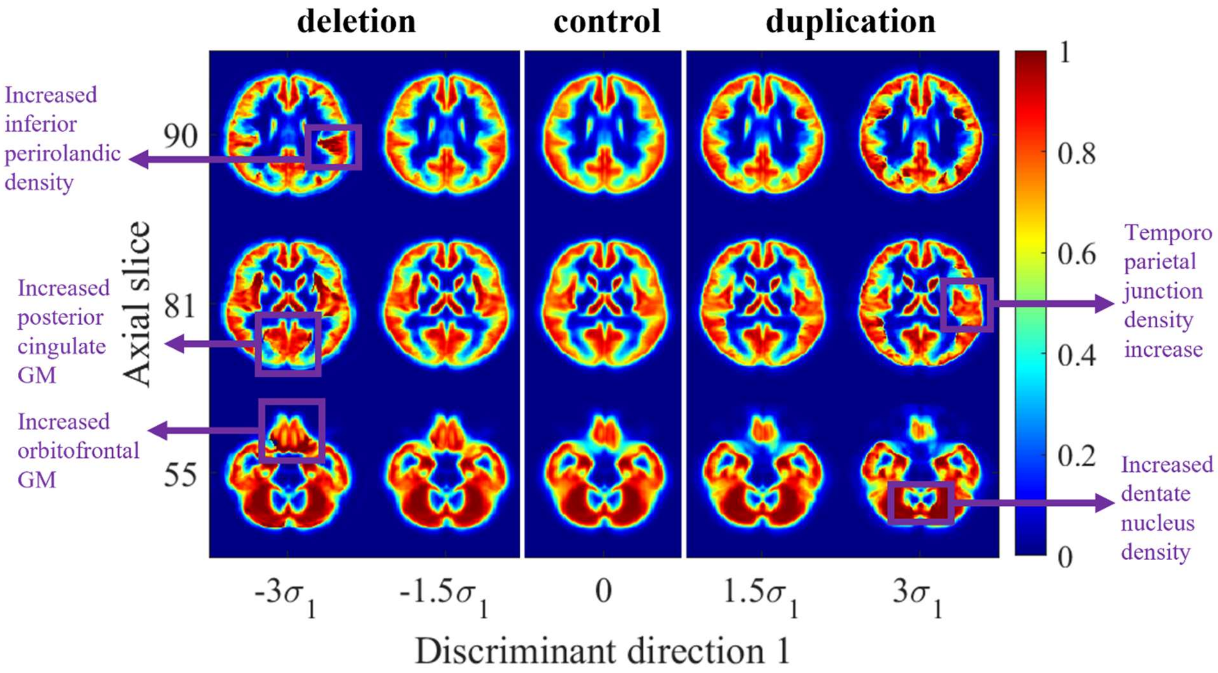

Figure S7. Gray matter. These computer-generated images can then be interpreted to understand the differences that enable high classification accuracy by visualizing along discriminant direction 1. Color represents tissue density. Here, σ_1 is the standard deviation from the mean (represented by score 0). The axial slices best showing the changes in gray matter morphology are shown.

Slice 55 shows increased gray matter density in the orbitofrontal regions (deletion carriers > controls > duplication carriers). Furthermore, there are changes in gray matter density in the dentate nucleus of the cerebellum (duplication carriers > controls > deletion carriers). Slice 81 shows changes in gray matter density in the insular regions (deletion carriers > controls > duplication carriers) as well as in the temporoparietal junction (deletion carriers < controls < duplication carriers). Furthermore, the posterior cingulate shows changes as well (deletion carriers > controls > duplication carriers). Finally, slice 90 shows that gray matter density in the inferior perirolandic areas are affected as well (duplication carriers < controls < deletion carriers) with left showing more changes than the right.

S5. Effect of confounding variables on TBM pLDA discrimination

As deletion carriers were younger than both duplication carriers and controls, the pLDA discriminant was computed after removing the influence of confounding variables of age and gender on the TBM maps according to Eq. S1.

$$V = D - Z(Z^T Z)^{-1} Z^T D \qquad \text{Eq. S1}$$

Here, $Z \in \mathbb{R}^{n \times c}$, which is the matrix containing *c* covariates and *n* is the number of subjects. *D* corresponds to the original data matrix before dimensionality reduction and *V* is the residual data matrix that is uncorrelated and orthogonal to the confounding variables. PCA was performed for dimensionality reduction, retaining the components capturing 96% of the variance as in the main text, followed by classification using pLDA, which yields the following plots in Figure S8.

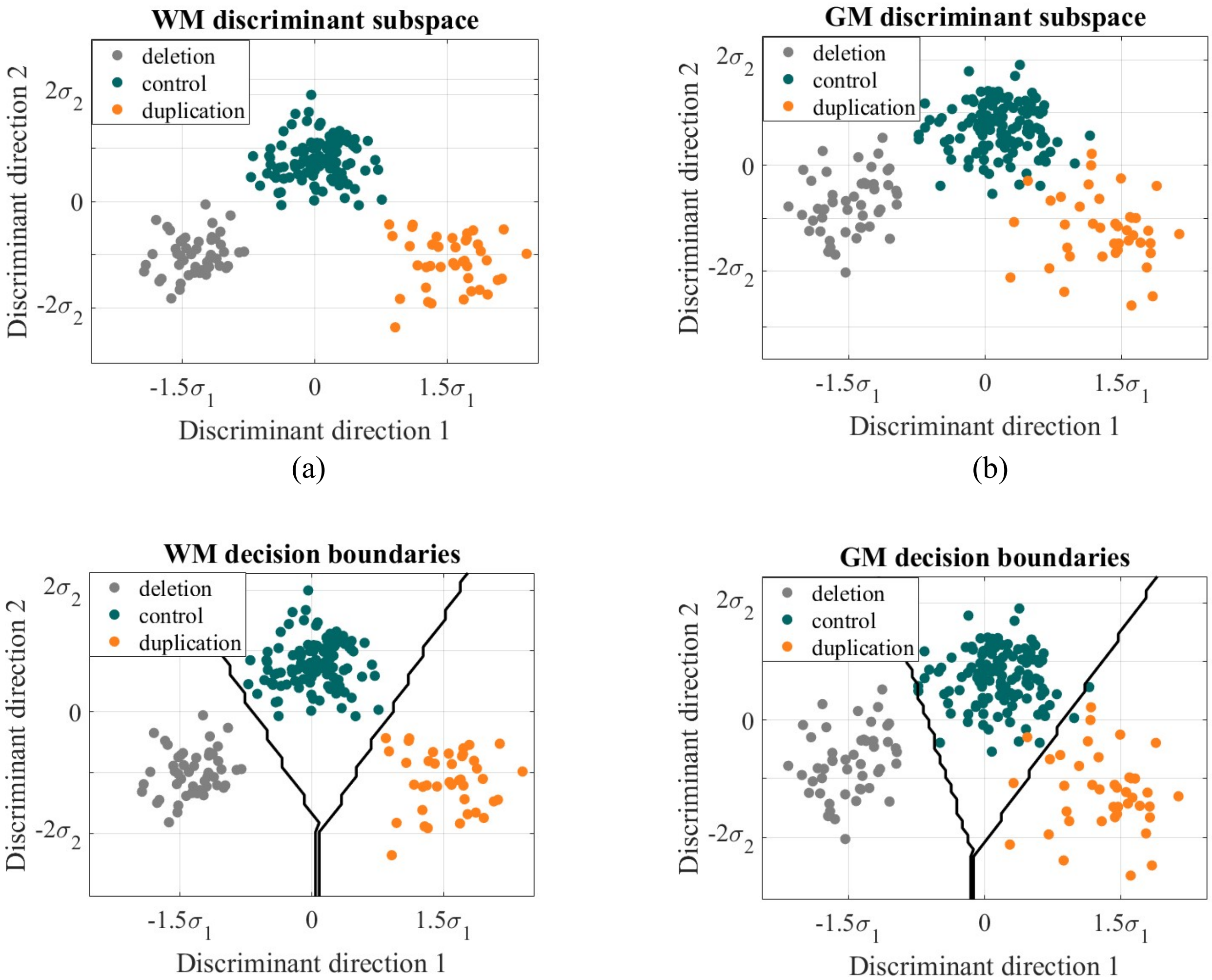

(a) (b)

(c) (d)

Figure S8. 3D TBM discriminant subspace, corrected for influence of age and gender. Each subject in the study is represented by a point on the scatter plot. Subject data projected onto the most discriminant subspace computed by pLDA for (a) white matter and (b) gray matter. Boundaries between the classes computed based on nearest centroid classification for (c) white matter and (d) gray matter.

10-fold stratified repeated cross validation was performed to obtain the test accuracy and confidence intervals using the same folds as in the main text. Results are summarized in Table S2.

Table S2. TBM classification accuracies corrected for age and gender

Features	**Test accuracy**	**Sensitivity** ***(deletion/control/ duplication)***	**Specificity** ***(deletion/control/ duplication)***	**Cohen's kappa**
White matter TBM (corrected)	88.9 [86.9, 90.8]%	89.7 [87.9, 91.6]% / 92.9 [91.3, 94.5]% / 76.0 [73.4, 78.7]%	96.5 [95.3, 97.6]% / 84.4 [82.1, 86.6]% / 97.9 [97.0, 98.8]%	0.81 [0.78, 0.83]
Gray matter TBM (corrected)	86.7 [84.6, 88.8]%	91.0 [89.2, 92.8]% / 88.9 [87.0, 90.9]% / 74.8 [72.1, 77.5]%	96.1 [94.9, 97.3]% / 83.9 [81.6, 86.1]% / 95.7 [94.5, 97.0]%	0.77 [0.74, 0.80]

Thus, TBM demonstrated robust classification performance even after controlling for age and gender through a covariate-controlled experiment, suggesting reliable individual classification.

S6. Combined gray and white matter penalized linear discriminant analysis

As gray matter and white matter contain partially independent information, the pLDA technique was applied to the concatenated gray and white matter data matrix. The top 96% of the variance in the combined dataset was captured by 83 components. The resulting discriminant subspace in Figure S9 again demonstrates that the classes are highly separable, although with minimally increased intra-class variance compared to white matter alone.

a.

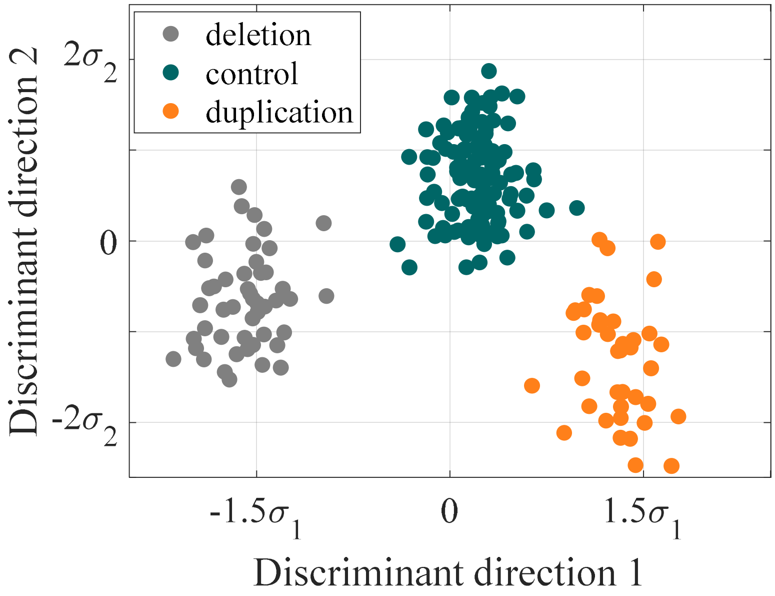

b.

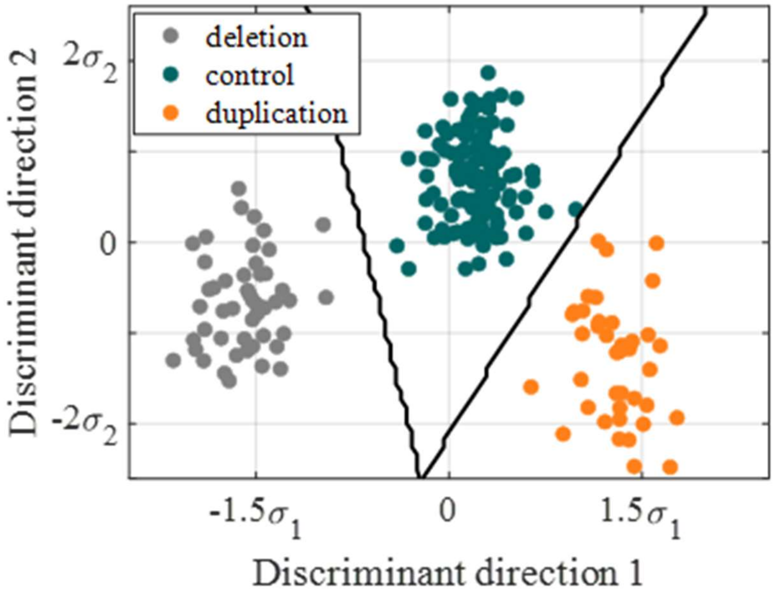

Figure S9. The CNV cohorts remain separable when gray matter and white matter are concatenated into a single data matrix

S7. Image domain representation versus transport-domain representation

S7.1 PCA variance plots

Images were smoothed and padded to enable direct comparison to the TBM processing pipeline in the main manuscript.

For white matter structural images, 96% of the variance in the dataset is captured by 132 components in the transport domain, 183 components using modulated SPM, 189 components using unmodulated SPM, and 184 components in the image domain.

For gray matter structural images, 96% of the variance in the dataset is captured by 46 components in the transport domain, 181 components using modulated SPM, 188 components using unmodulated SPM, and 182 components in the image domain.

a.

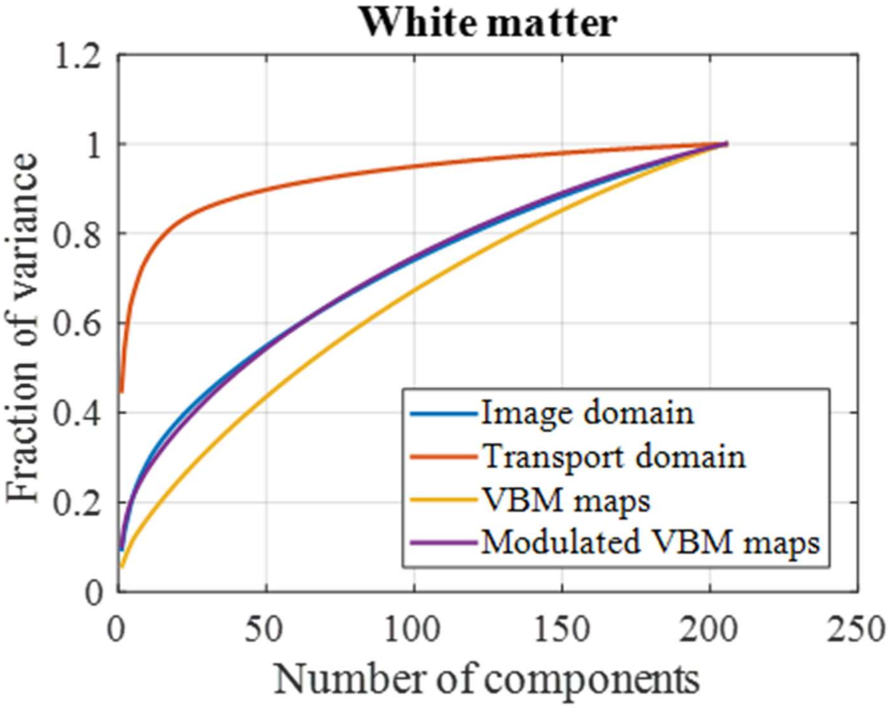

b.

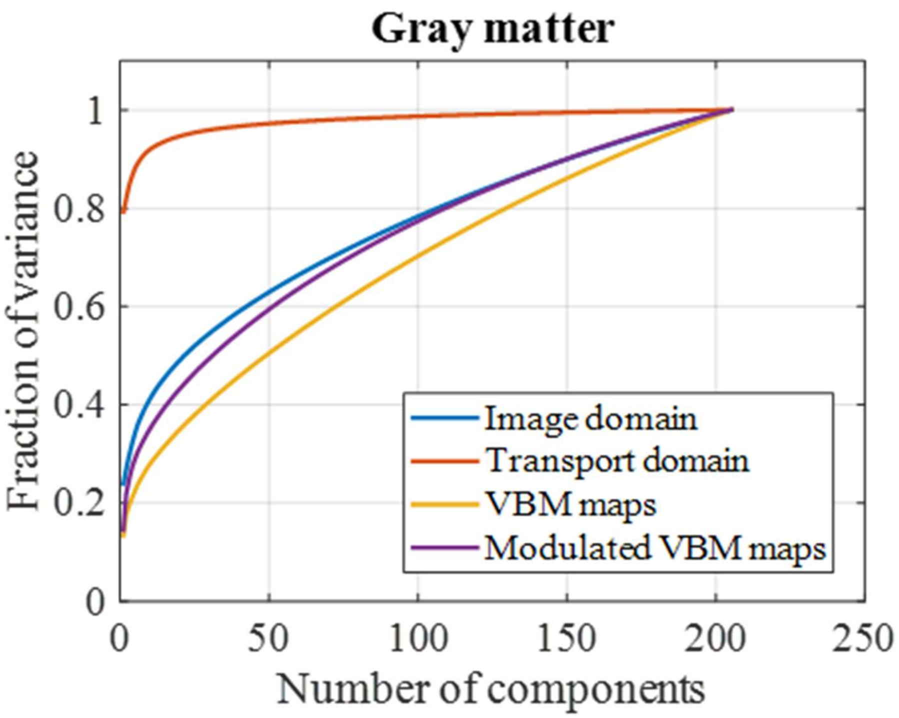

Figure S10. Transport-based morphometry best captures brain structural variations compared to other modeling techniques for both white matter (a) and gray matter (b) images. TBM requires the fewest principal components to explain the variance in the dataset.

Figure S10 illustrates that the transport domain offers strong modeling advantages compared to other registration-based techniques.

S8. Template change

In prior work, substituting a smooth template with a different nearest neighbor template did not significantly increase or decrease discrimination accuracy [20]. We demonstrate this in Figure S11. A new template was computed from 172 healthy individuals aged 58-81 from a separate study published in [22]. Then, the current study population images were registered to this template [22], following affine registration to match the gross orientation and scaling of the images in the cohort. As Figure S11 demonstrates, changing the template does not modify class separability.

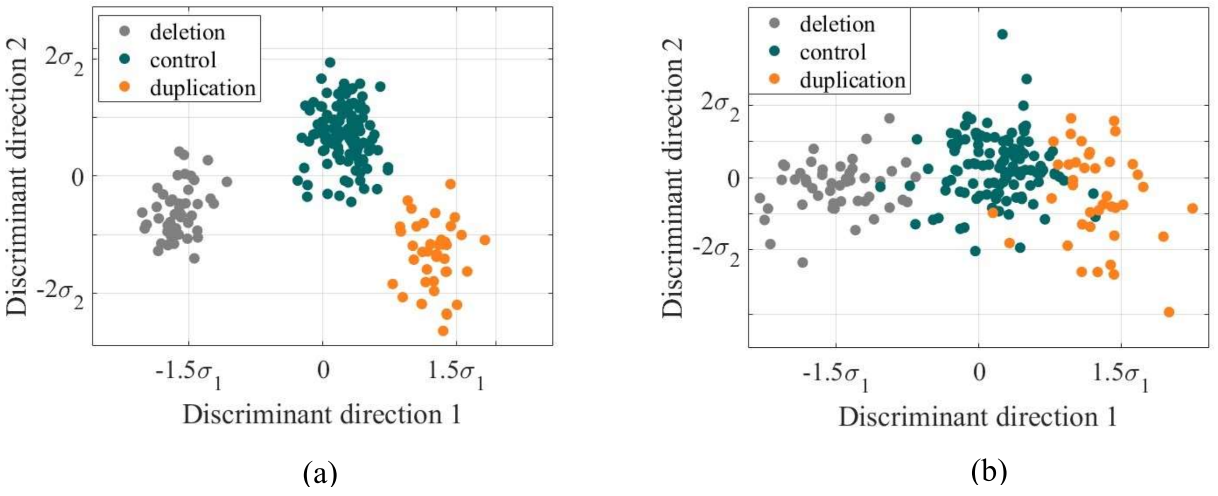

Figure S11. pLDA discriminant subspace calculated for (a) white matter and (b) gray matter

S9. Harvard-Oxford atlas registration

a.

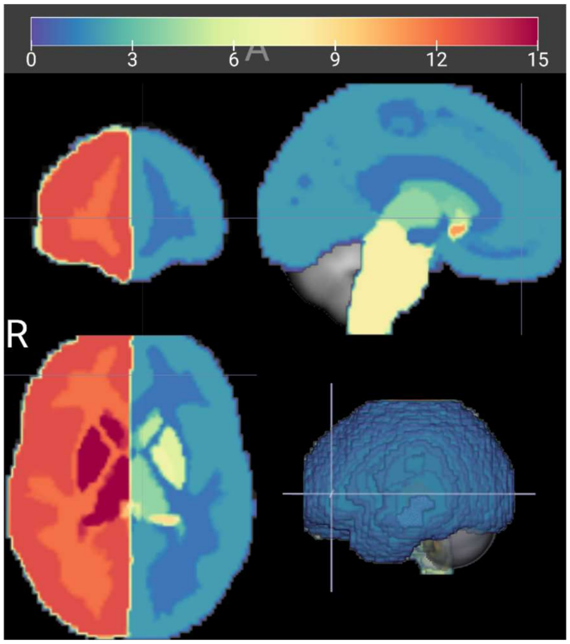

b.

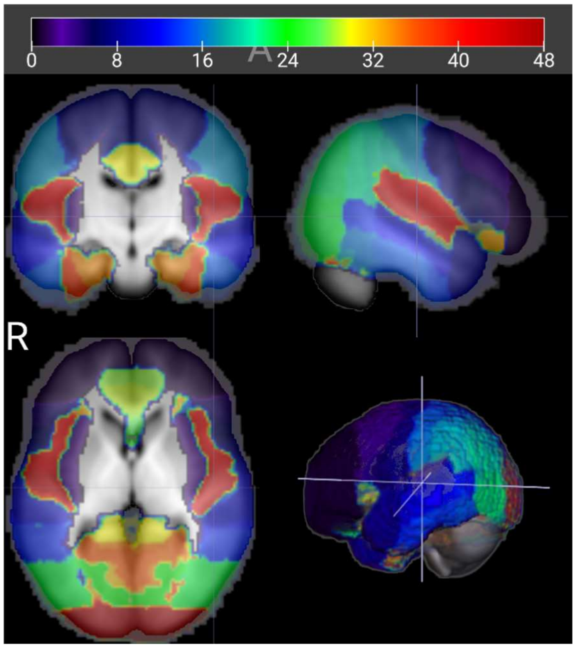

Figure S12. (a) Cortical segmentation and (b) subcortical segmentation of the population mean image via the Harvard-Oxford atlas

After the Harvard-Oxford atlas is registered to the population mean image, the segmentations for cortical and subcortical segmentation are shown in Figure S12.

S10. Supplementary Text

S10.1 HDLSS Data

Nonlinear classifiers are prone to overfitting in high-dimensional low sample size (HDLSS) problems, and the variance of the classifier increases as the classifier becomes more complex. This is a limitation of large neural networks.

Here, 3D TBM can model nonlinear distances in the image domain as Euclidean distances in the transport domain. Thus, we can use a linear classifier, which offers several advantages. First, is efficient implementation. Next, linear classifiers have a favorable bias-variance tradeoff, especially for high –dimensional data [65].

S10.2 TBM: generative modeling

Generative modeling offers a way to interpret opaque machine learning models. As generative modeling produces plausible instances of the data, we can generate representative data samples through TBM synthesis, which can be written in closed form (Equation 3). In contrast to other generative techniques, 3D TBM is physics-based and captures the transport phenomenon and is convex, offering a unique solution. This allows for direct physical interpretation.

Traditional quantitative morphometry approaches [58-60, 63-64] also suffer from the inability to recover the physical substrates underlying the associations between quantitative metrics (i.e. brain volume, cortical thickness, shape descriptors, etc.) and genetic cohort. These metrics are reductive and physical shifts in morphologic profile cannot be recovered from these descriptors alone, i.e. they are not *generative*.

A key advance of 3D TBM as a predictive model is the ability to directly visualize and interpret the tissue shifts driving classification. Unfortunately, traditional methods that rely on extracting a set of numerical descriptors such as volume, thickness, etc. from the images or those that rely on voxelwise comparison are non-invertible transformations. Indeed, the creators of voxel-based morphometry summarize: "in [predictive] models, the parameters have no physical meaning unless the corresponding generative model [used to explain the data] is invertible" [18].

S10.3 Image domain

To compare to TBM classification, image domain classification was performed both for whole brain and for individual tissue maps. First, raw whole brain images were affine registered to correct for gross orientational and size differences and skull stripped. Then, they were smoothed and normalized similar to the preprocessing steps for the individual gray and white matter maps. After dimensionality reduction using PCA, retaining 96% of the variance, the discriminant subspace was computed in the training set using pLDA, with scatter plots displayed in Figure S13.

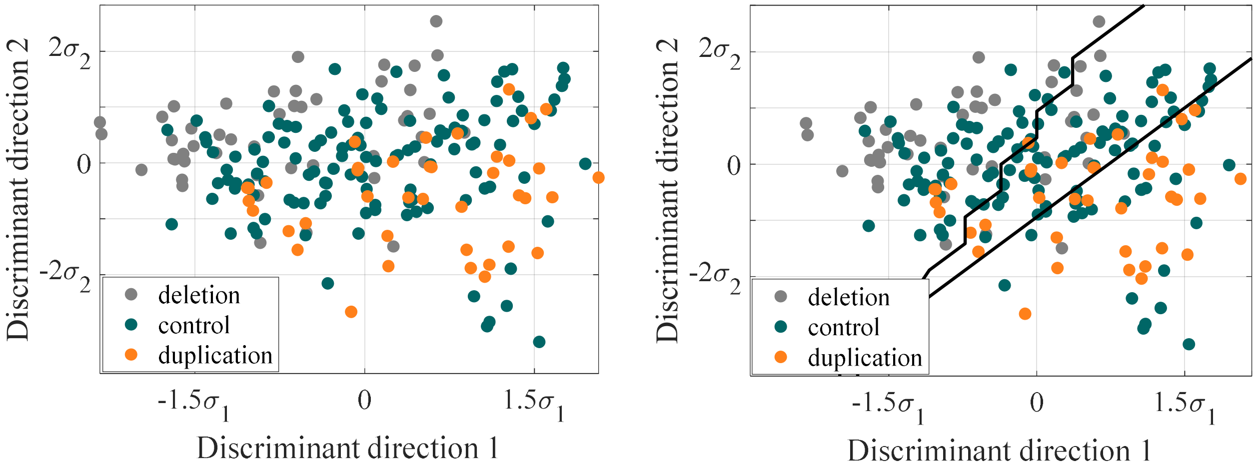

(a) (b)

Figure S13. Whole brain image domain discriminant subspace after affine registration, intensity normalization, and smoothing. Each subject in the study is represented by a point on the scatter plot. Subject data projected onto (a) the most discriminant subspace computed by pLDA. (b) boundaries between the classes computed based on nearest centroid classification

The classification accuracies are computed after stratified repeated 10-fold cross validation with the same folds as in the main text. Results are in Table S3. The original whole brain images were separable with accuracy comparable to chance.

Table S3. Image domain classification accuracies, whole brain

Features	Test accuracy	Sensitivity (deletion/control/ duplication)	Specificity (deletion/control/ duplication)	Cohen's kappa
Whole brain (normalized)	53.6 [50.5, 56.7]%	65.9 [63.0, 68.9]% / 47.1 [44.0, 50.2] % / 58.1 [55.1, 61.2]%	75.9 [73.3, 78.6]% / 68.4 [65.5, 71.3]% / 82.1 [79.8, 84.5] %	0.27 [0.25, 0.30]

Next, the discriminant ability of the preprocessed affine registered gray and white matter tissue maps was assessed. PCA analysis was run on these maps, retaining the components capturing the top 96% of the variance, as in the main TBM analysis. The scatter plots in Figure S14 demonstrate the pLDA discriminants in the training space.

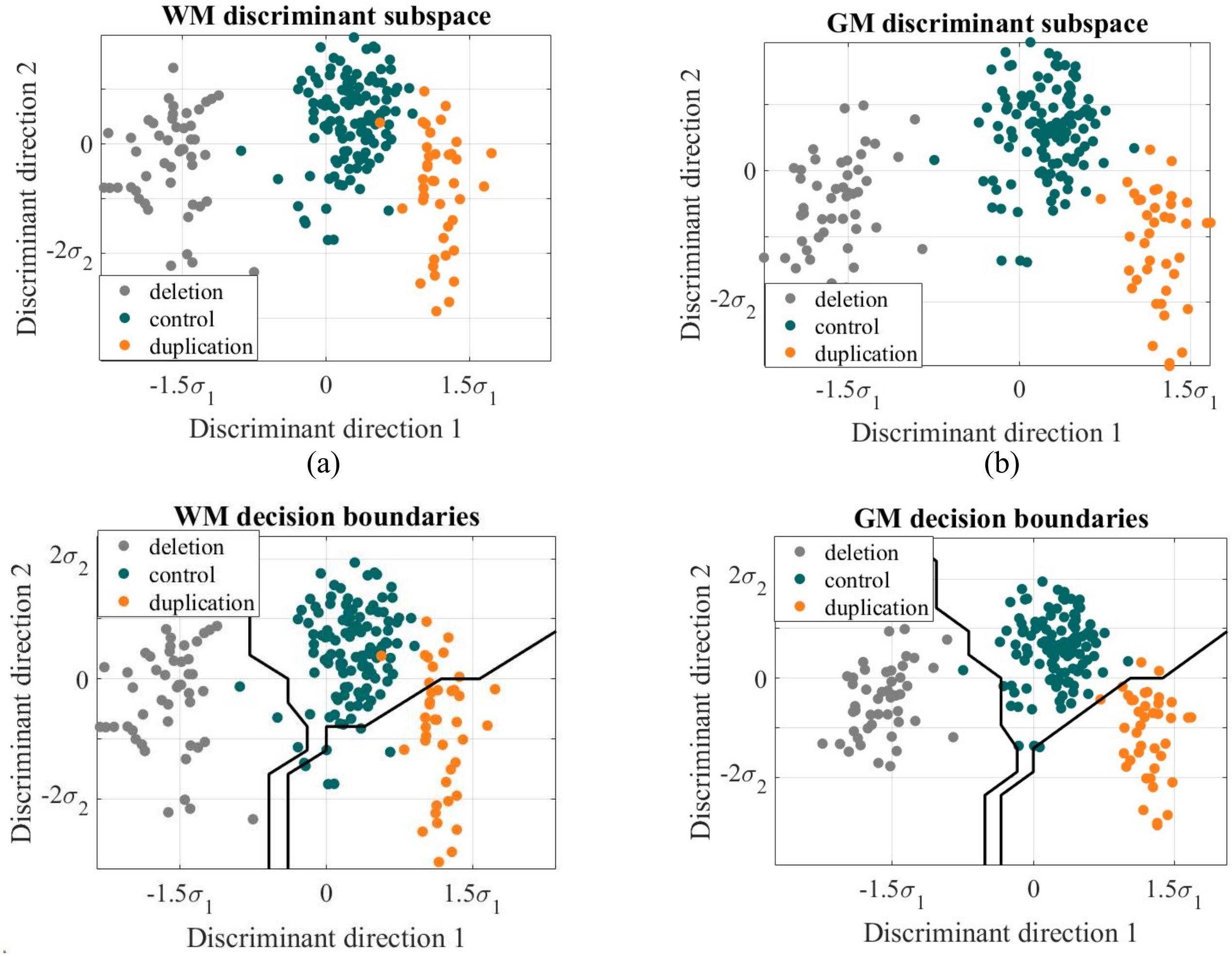

(a) (b)

(c) (d)

Figure S14. Gray and white matter preprocessed images. Each subject in the study is represented by a point on the scatter plot. Subject data projected onto the most discriminant subspace computed by pLDA for (a) white matter and (b) gray matter. Boundaries between the classes computed based on nearest centroid classification for (c) white matter and (d) gray matter.

Stratified repeated 10-fold cross validation was performed to obtain the test accuracy and confidence intervals as described in the main text. Results are summarized in Table S4. These results underscore the effectiveness of our preprocessing steps of affine registration, segmentation, and normalization on the original images. TBM further improves upon these classification accuracies by up to 10% by capturing the nonlinear information not well-assessed in the image domain alone (Table 3).

Table S4. Image domain classification accuracies, separate white and gray matter

Features	**Test accuracy**	**Sensitivity (deletion/control/ duplication)**	**Specificity (deletion/control/ duplication)**	**Cohen's kappa**
WM tissue maps (normalized)	84.9 [82.7, 87.1]%	95.0 [93.6, 96.3]% / 89.3 [87.4, 91.2]% / 59.9 [56.9, 63.0]%	97.2 [96.2, 98.2]% / 80.2 [77.7, 82.6]% / 94.4 [93.0, 95.9]%	0.74 [0.71, 0.76]
GM tissue maps (normalized)	87.7 [85.6, 89.7]%	91.7 [90.0, 93.4]% / 92.8 [91.2, 94.4]% / 67.8 [64.9, 70.7]%	97.8 [96.9, 98.7]% / 80.8 [78.4, 83.3]% / 96.9 [95.9, 98.0]%	0.78 [0.76, 0.81]

Finally, the model was interrogated to visualize the changes driving classification ability in the image domain, directly comparable to Figure S7 generated by TBM.

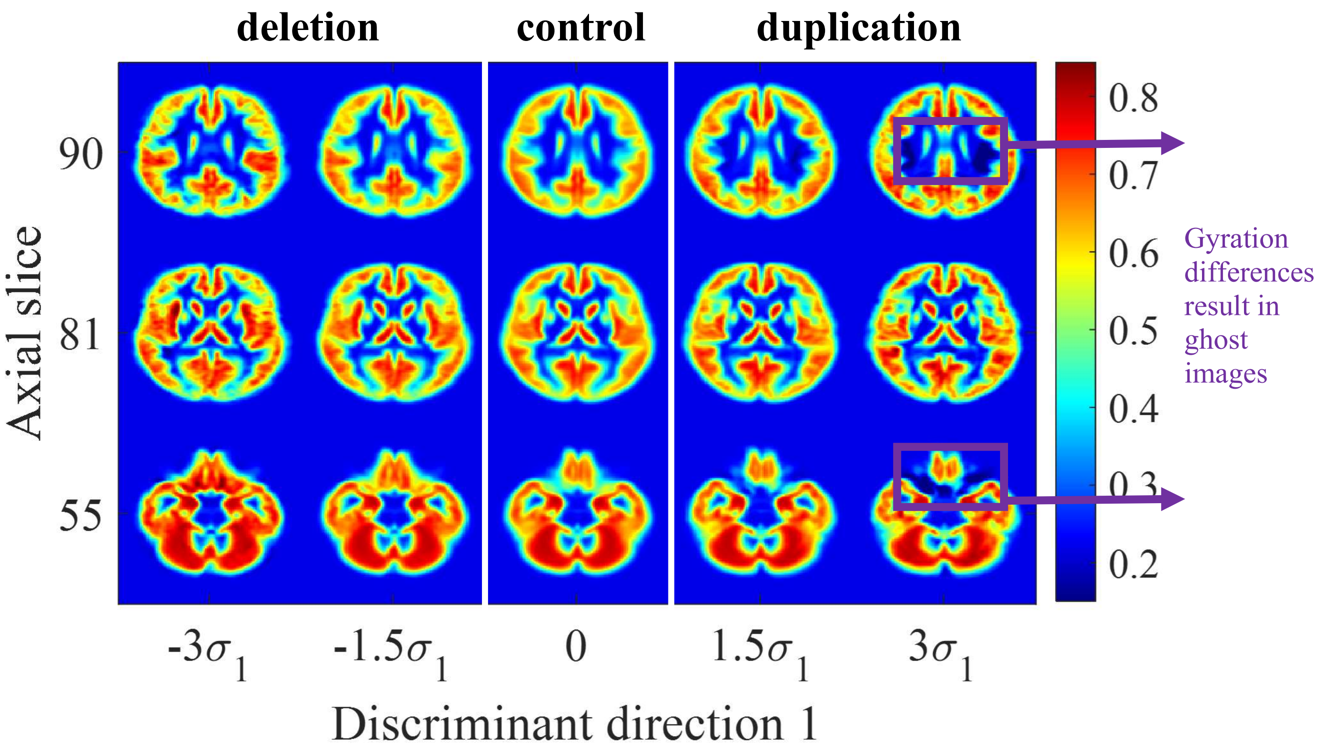

Gyration differences result in ghost images

Figure S15. Gray matter. Synthetic images generated by interrogating the image domain model along direction 1. Linear voxelwise comparison can assess presence of differences in spatial gray matter to some degree, however, the ghost images are seen where differences are present. Color represents normalized tissue intensity. Here, σ_1 is the standard deviation from the mean (represented by score 0).

Figure S15 demonstrates that although the image domain model leveraging voxelwise comparison can detect spatial differences in gray matter to some degree, it is not sufficiently sensitive to nonlinear patterns such as gyral folding. This limitation is evidenced by the presence of ghost image where gyri are not comparable in a voxelwise manner. In contrast, Figure S7 highlights the strength of TBM in elegantly capturing and visualizing nonlinear changes in tissue distribution such as gyration.

Several factors could explain why separating gray and white matter tissues improves classification performance. First, combining these tissues in a whole brain image might lead to destructive interference, where opposing signals from gray and white matter changes cancel out. Second, changes may be tissue-specific, meaning that they primarily affect either gray matter or white matter. Isolating each tissue compartment allows the model to focus on the tissue-specific changes, leading to better discrimination. Third, segmenting the whole brain into gray and white matter effectively reduces data dimensionality, which improves classification performance.

S10.4 Voxel-based morphometry

On the preprocessed images, further statistical parametric maps were generated for gray matter and white matter structural images separately. The standard VBM8 toolbox in the Statistical Parametric Mapping software version 12 was used.

S10.5 Deformation-based morphometry

Unlike with transport-based morphometry, the deformation field is not unique for a pair of images; thus, many possible deformation fields may exist between images and the statistical results may vary depending as a function of the field rather than solely the two images of interest. The deformation fields were computed using the standard VBM8 toolbox from the affinely registered images to enable appropriate comparison with 3D TBM. The standard VBM8 toolbox was used for the computations above.

S10.6 Penalized linear discriminant analysis with voxel-based maps

To enable comparison to discrimination ability with the TBM technique, VBM and DBM maps were generated according to the procedure in *S10.4* and *S10.5.* Then, stratified 10-fold cross-validation was performed using the same code as that for 3D TBM classification analysis. The results are summarized in Tables S5A and S5B.

Table S5. Classification accuracies using pLDA

A.

Features	**Test accuracy**	**Sensitivity (deletion / control/ duplication)**	**Specificity (deletion / control/ duplication)**	**Cohen's kappa**
GM tissue maps (unmodulated)	84.9 [82.7, 87.1]%	84.3 [82.1, 86.6]/ 99.2 [98.7, 99.8]/ 43.3 [40.3, 46.4]%	99.7 [99.3, 100]/ 65.7 [62.7, 68.6]/ 99.8 [99.5, 100]%	0.71 [0.69, 0.74]
WM tissue maps (unmodulated)	84.2 [82.0, 86.5]%	82.1 [79.7, 84.5]/ 99.6 [99.2, 100]/ 41.5 [38.5, 44.6]%	100 [100, 100]/ 63.6 [60.7, 66.6]/ 99.7 [99.4, 100]%	0.70 [0.67, 0.73]
GM tissue maps (modulated)	71.0 [68.2, 73.8]%	83.9 [81.6, 86.2]/ 71.3 [68.5, 74.1]/ 54.8 [51.7, 57.8]%	97.7 [96.7, 98.6]/ 70.9 [68.1, 73.7]/ 81.7 [79.3, 84.1]%	0.51 [0.48, 0.55]
WM tissue maps (modulated)	72.5 [69.8, 75.3]%	81.7 [79.3, 84.1]/ 68.9 [66.0, 71.8]/ 72.3 [69.5, 75.0]%	96.1 [94.9, 97.3]/ 78.5 [76.0, 81.1]/ 81.0 [78.6, 83.4]%	0.55 [0.52, 0.58]

B.

Features	**Test accuracy**	**Sensitivity (deletion / control / duplication)**	**Specificity (deletion /control duplication)**	**Cohen's kappa**
Deformation fields	93.4 [91.9, 95.0]%	95.7 [94.4, 96.9]/ 95.6 [94.3, 96.8]/ 84.5 [82.2, 86.7]%	98.7 [98.1, 99.4]/ 90.6 [88.8, 92.4]/ 98.0 [97.2, 98.9]%	0.89 [0.87, 0.91]

Thus, compared to other techniques assessing nonlinear information, TBM achieved higher classification accuracies of up to 22% for white matter and 17% for gray matter.

S11. Regional mean displacements based on Harvard-Oxford atlas

As described in the main text, the Harvard-Oxford atlas was co-registered to the template image and TBM displacements were analyzed on a regional basis. Regional volume contraction/dilation beyond mean displacements was calculated as the determinant of the Jacobian of the transport maps. Z-scores were calculated regarding degree of local regional volume expansion (positive) or contraction (negative). The classifier was interrogated at three standard deviations away from the mean image for duplication carriers and deletion carriers, either along direction 1 or direction 2, corresponding to the discriminant subspaces in Figure 2. The average voxelwise Z scores per region are summarized in Table S6 through Table S9.

Generally, every region queried by the atlas undergoes local change – suggesting diffuse rather than local perturbations due to 16p11.2 genotype. Second, we confirm that there are reciprocal changes between duplication/deletion carriers given overlapping regions of change, but in different direction with gene dosage. Third, the areas undergoing the largest local volume contraction or expansion do not necessarily conform with known anatomic brain networks, again supporting the observation of a diffuse rather than network-specific perturbation.

Table S6. Direction 1 – Z-scores of cortical regions

	Deletion carriers	**Duplication carriers**
1. Frontal pole	-0.02	0.01
2. Insular cortex	-0.09	0.06
3. Superior frontal gyrus	0.05	-0.06
4. Middle frontal gyrus	0.08	-0.09
5. Inferior frontal gyrus (pars triangularis)	-0.06	0.06
6. Inferior frontal gyrus (pars opercularis)	0.47	-0.50
7. Precentral gyrus	0.12	-0.12
8. Temporal pole	0.29	-0.29
9. Superior temporal gyrus (anterior division)	0.21	-0.23
10. Superior temporal gyrus (posterior division)	0.06	-0.06
11. Middle temporal gyrus (anterior division)	-0.01	0
12. Middle temporal gyrus (posterior division)	0.26	-0.22
13. Middle temporal gyrus (temporooccipital part)	0.31	-0.26
14. Inferior temporal gyrus (anterior division)	0.10	-0.11
15. Inferior temporal gyrus (posterior division)	-0.36	0.38

16. Inferior temporal gyrus (temporooccipital part)	0.04	-0.07
17. Postcentral gyrus	-0.02	0.02
18. Superior parietal lobule	-0.25	0.24
19. Supramarginal gyrus (anterior division)	0.05	-0.08
20. Supramarginal gyrus (posterior division)	0.11	-0.13
21. Angular gyrus	0.35	-0.32
22. Lateral occipital cortex (superior division)	0.13	-0.14
23. Lateral occipital cortex (inferior division)	0.11	-0.13
24. Intracalcarine cortex	-0.85	1.02
25. Frontal medial cortex	-0.25	0.20
26. Juxtapositional lobule cortex (formerly supplementary motor cortex)	-0.05	0.03
27. Subcallosal cortex	-0.09	0.12
28. Paracingulate gyrus	-0.04	0.02
29. Cingulate gyrus (anterior division)	0.40	-0.39
30. Cingulate gyrus (posterior division)	0.25	-0.23
31. Precuneous cortex	-0.23	0.24
32. Cuneal cortex	0.12	-0.18
33. Frontal orbital cortex	-0.35	0.35
34. Parahippocampal gyrus (anterior division)	-0.20	0.20
35. Parahippocampal gyrus (posterior division)	0.27	-0.27
36. Lingual gyrus	0.04	-0.07
37. Temporal fusiform cortex (anterior division)	-0.06	0.05
38. Temporal fusiform cortex (posterior division)	-0.01	-0.02
39. Temporal occipital fusiform cortex	0.04	-0.06
40. Occipital fusiform gyrus	-0.04	-0.01
41. Frontal operculum cortex	-0.63	0.64
42. Central opercular cortex	-0.85	0.89
43. Parietal operculum	-0.88	0.96
44. Planum polare	-0.04	-0.03
45. Heschl’s gyrus (includes H1 and H2)	0.09	-0.15
46. Planum temporale	0.11	-0.17
47. Supracalcarine cortex	-0.55	0.41
48. Occipital pole	-0.07	0.06

Table S7. Direction 1 – Z scores of subcortical regions (deep gray matter and white matter†)

	Deletion carriers	Duplication carriers
1. Left cerebral white matter†	0.08	-0.11
2. Left cerebral cortex	-0.04	0.03
3. Left lateral ventricle†	-0.06	0.05
4. Left thalamus	-0.06	0.04
5. Left caudate	0.32	-0.33
6. Left putamen	0.16	-0.21
7. Left pallidum	0.06	-0.03
8. Brain stem†	0.09	-0.08
9. Left hippocampus	-0.05	0.05
10. Left amygdala	-0.03	0
11. Left accumbens	0.15	-0.19
12. Right cerebral white matter†	0.06	-0.08
13. Right cerebral cortex	-0.10	0.10
14. Right lateral ventricle†	-0.08	0.07
15. Right thalamus	-0.16	0.14
16. Right caudate	0.03	-0.05
17. Right putamen	0.14	-0.18
18. Right pallidum	0.11	-0.10
19. Right hippocampus	-0.02	0.01
20. Right amygdala	0.03	-0.05
21. Right accumbens	0.08	-0.11

Table S8. Direction 2 – Z-scores of cortical regions

	Deletion/Duplication carriers	Controls
1. Frontal pole	0.12	-0.12
2. Insular cortex	0.27	-0.27
3. Superior frontal gyrus	-0.05	0.05
4. Middle frontal gyrus	-0.05	0.05
5. Inferior frontal gyrus (pars triangularis)	0.26	-0.26
6. Inferior frontal gyrus (pars opercularis)	-0.12	0.12
7. Precentral gyrus	-0.02	0.01
8. Temporal pole	-0.35	0.36
9. Superior temporal gyrus (anterior division)	-0.58	0.62
10. Superior temporal gyrus (posterior division)	0.11	-0.11

11. Middle temporal gyrus (anterior division)	-0.37	0.38
12. Middle temporal gyrus (posterior division)	0.26	-0.25
13. Middle temporal gyrus (temporooccipital part)	0.22	-0.23
14. Inferior temporal gyrus (anterior division)	-0.04	0.05
15. Inferior temporal gyrus (posterior division)	0.23	-0.22
16. Inferior temporal gyrus (temporooccipital part)	0.43	-0.41
17. Postcentral gyrus	0.24	-0.24
18. Superior parietal lobule	0.22	-0.22
19. Supramarginal gyrus (anterior division)	0.50	-0.49
20. Supramarginal gyrus (posterior division)	0.40	-0.38
21. Angular gyrus	0.29	-0.31
22. Lateral occipital cortex (superior division)	0.02	-0.02
23. Lateral occipital cortex (inferior division)	0.08	-0.08
24. Intracalcarine cortex	-0.05	0.05
25. Frontal medial cortex	0	-0.01
26. Juxtapositional lobule cortex (formerly supplementary motor cortex)	-0.03	0.03
27. Subcallosal cortex	0.20	-0.18
28. Paracingulate gyrus	-0.06	0.05
29. Cingulate gyrus (anterior division)	0.08	-0.09
30. Cingulate gyrus (posterior division)	-0.26	0.27
31. Precuneous cortex	-0.15	0.14
32. Cuneal cortex	0.20	-0.19
33. Frontal orbital cortex	0.61	-0.60
34. Parahippocampal gyrus (anterior division)	0.17	-0.17
35. Parahippocampal gyrus (posterior division)	0.07	-0.08
36. Lingual gyrus	0.07	-0.08
37. Temporal fusiform cortex (anterior division)	0.14	-0.14
38. Temporal fusiform cortex (posterior division)	0.13	-0.14
39. Temporal occipital fusiform cortex	0.06	-0.07
40. Occipital fusiform gyrus	0.19	-0.19

41. Frontal operculum cortex	-0.09	0.05
42. Central opercular cortex	0.15	-0.18
43. Parietal operculum	0.05	-0.06
44. Planum polare	0.15	-0.18
45. Heschl's gyrus (includes H1 and H2)	0.11	-0.13
46. Planum temporale	0.21	-0.18
47. Supracalcarine cortex	0.41	-0.41
48. Occipital pole	0.19	-0.18

Table S9. Direction 2 – Z scores of subcortical regions (deep gray matter and white matter†)

	Deletion/Duplication carriers	**Controls**
1. Left cerebral white matter†	0.08	-0.10
2. Left cerebral cortex	0.10	-0.10
3. Left lateral ventricle†	-0.16	0.18
4. Left thalamus	0.20	-0.20
5. Left caudate	0.29	-0.30
6. Left putamen	0.06	-0.07
7. Left pallidum	0.07	-0.05
8. Brain stem†	0.06	-0.07
9. Left hippocampus	0.50	-0.50
10. Left amygdala	0.16	-0.17
11. Left accumbens	0.16	-0.19
12. Right cerebral white matter†	0.13	-0.14
13. Right cerebral cortex	0.09	-0.09
14. Right lateral ventricle†	-0.31	0.33
15. Right thalamus	0.07	-0.07
16. Right caudate	0.69	-0.68
17. Right putamen	0.14	-0.15
18. Right pallidum	0.54	-0.53
19. Right hippocampus	0.40	-0.39
20. Right amygdala	0.25	-0.26
21. Right accumbens	0.19	-0.25

Networks most affected appear to include the salience network, visual system, association areas, mixed motor/sensory function, object recognition, language areas, and visual word/faces recognition. The heterogeneity of networks affected mirrors the heterogeneity of phenotypic presentations summarized in Table 2 in the main text.

S12. Summary

In summary, the transport-based morphometry (3D TBM) [19, 21, 24] technique is generative and enables visualization of the structural changes responsible for sensitive prediction, overcoming a major obstacle in extracting physical meaning from statistical results. While traditional brain morphometry analysis focuses on explaining the given dataset [18], the 3D TBM technique is an avenue for predictive modeling, where modern data-driven machine learning techniques can be utilized to construct models that can accurately predict the characteristics of new data. Several studies have shown that complex, nonlinear, and spatially diffuse patterns can be represented sparsely in the transport space [19, 21, 24, 61].

Canonical correlation analysis investigating the relationship between the gray matter and white matter variance finds that 31% of the variance can be mutually explained. The findings are compatible with [44], who observed a power law relating how the relative volumes of gray matter and white matter scale. However, this power law does not explicitly model the connectivity and cortical folding [44], which likely contributes to the remainder of the variance. Furthermore, the finding that combining gray matter and white matter do not increase discriminant capability is an expected finding may potentially be explained collinearity of gray matter and white matter tissue.

By discovering and visualizing information that is non-visible to the human eye, 3D TBM addresses long-standing limitations in understanding the gene-brain-behavior relationship**.** We envision that this technique can accelerate progress in precision medicine for a variety of diseases.

With the ability to reveal subtle morphologic variations that may be associated with genetic variations, 3D TBM has the potential to inform personalized diagnosis, treatment, and monitoring strategies for individuals with neurologic and psychiatric disorders.

REFERENCES AND NOTES

1. D. H. Geschwind, Genetics of autism spectrum disorders. *Trends Cogn. Sci.* **15**, 409–416 (2011).

2. American Psychiatric Association, What is autism spectrum disorder?, https://psychiatry.org/patients-families/autism/what-is-autism-spectrum-disorder (2023). [accessed 18 November 2023].

3. E. B. Binder, Genotype-phenotype predictions in autism: Are we there yet?. *Am. J. Psychiatry* **178**, 11–12 (2021).

4. S. Sandin, P. Lichtenstein, R. Kuja-Halkola, C. Hultman, H. Larsson, A. Reichenberg, The heritability of autism spectrum disorder. *JAMA* **318**, 1182–1184 (2017).

5. A. Speaks, Should I or we have genetic testing for autism? Expert Opinion (2023).

6. J. M. Fu, F. K. Satterstrom, M. Peng, H. Brand, R. L. Collins, S. Dong, B. Wamsley, L. Klei, L. Wang, S. P. Hao, C. R. Stevens, C. Cusick, M. Babadi, E. Banks, B. Collins, S. Dodge, S. B. Gabriel, L. Gauthier, S. K. Lee, L. Liang, A. Ljungdahl, B. Mahjani, L. Sloofman, A. N. Smirnov, M. Barbosa, C. Betancur, A. Brusco, B. H. Y. Chung, E. H. Cook, M. L. Cuccaro, E. Domenici, G. B. Ferrero, J. J. Gargus, G. E. Herman, I. Hertz-Picciotto, P. Maciel, D. S. Manoach, M. R. Passos-Bueno, A. M. Persico, A. Renieri, J. S. Sutcliffe, F. Tassone, E. Trabetti, G. Campos, S. Cardaropoli, D. Carli, M. C. Y. Chan, C. Fallerini, E. Giorgio, A. C. Girardi, E. Hansen-Kiss, S. L. Lee, C. Lintas, Y. Ludena, R. Nguyen, L. Pavinato, M. Pericak-Vance, I. N. Pessah, R. J. Schmidt, M. Smith, C. I. S. Costa, S. Trajkova, J. Y. T. Wang, M. H. C. Yu, The Autism Sequencing Consortium (ASC), B. Aleksic, M. Artomov, E. Benetti, M. Biscaldi-Schafer, A. D. Børglum, A. Carracedo, A. G. Chiocchetti, H. Coon, R. N. Doan, M. Fernández-Prieto, C. M. Freitag, S. Gerges, S. Guter, D. M. Hougaard, C. M. Hultman, S. Jacob, M. Kaartinen, A. Kolevzon, I. Kushima, T. Lehtimäki, C. L. Rizzo, N. Maltman, M. Manara, G. Meiri, I. Menashe, J. Miller, N. Minshew, M. Mosconi, N. Ozaki, A. Palotie, M. Parellada, K. Puura, A. Reichenberg, S. Sandin, S. W. Scherer, S. Schlitt, L. Schmitt, K. Schneider-Momm, P. M. Siper, P. Suren, J. A. Sweeney, K. Teufel, M. del Pilar Trelles, L. A. Weiss, R. Yuen, Broad Institute Center for Common Disease Genomics (Broad-CCDG), iPSYCH-BROAD Consortium, D. J. Cutler, S. de Rubeis, J. D. Buxbaum, M. J. Daly, B. Devlin, K. Roeder, S. J. Sanders, M. E. Talkowski, Rare

coding variation provides insight into the genetic architecture and phenotypic context of autism. *Nat. Genet.* **54**, 1320–1331 (2022).

7. A. Aglinskas, J. K. Hartshorne, S. Anzellotti, Contrastive machine learning reveals the structure of neuroanatomical variation within autism. *Science* **376**, 1070–1074 (2022).

8. M. H. Duyzend, X. Nuttle, B. P. Coe, C. Baker, D. A. Nickerson, R. Bernier, E. E. Eichler, Maternal modifiers and parent-of-origin bias of the autism-associated 16p11.2 cnv. *Am. J. Hum. Genet.* **98**, 45–57 (2016).

9. X. Nuttle, G. Giannuzzi, M. H. Duyzend, J. G. Schraiber, I. Narvaiza, P. H. Sudmant, O. Penn, G. Chiatante, M. Malig, J. Huddleston, C. Benner, F. Camponeschi, S. Ciofi-Baffoni, H. A. F. Stessman, M. C. N. Marchetto, L. Denman, L. Harshman, C. Baker, A. Raja, K. Penewit, N. Janke, W. J. Tang, M. Ventura, L. Banci, F. Antonacci, J. M. Akey, C. T. Amemiya, F. H. Gage, A. Reymond, E. E. Eichler, Emergence of a homo sapiens-specific gene family and chromosome 16p11.2 cnv susceptibility. *Nature* **536**, 205–209 (2016).

10. A. Y. Qureshi, S. Mueller, A. Z. Snyder, P. Mukherjee, J. I. Berman, T. P. Roberts, S. S. Nagarajan, J. E. Spiro, W. K. Chung, E. H. Sherr, R. L. Buckner, Simons VIP Consortium, Opposing brain differences in 16p11.2 deletion and duplication carriers. *J. Neurosci.* **34**, 11199–11211 (2014).

11. L. A. Weiss, Y. Shen, J. M. Korn, D. E. Arking, D. T. Miller, R. Fossdal, E. Saemundsen, H. Stefansson, M. A. Ferreira, T. Green, O. S. Platt, D. M. Ruderfer, C. A. Walsh, D. Altshuler, A. Chakravarti, R. E. Tanzi, K. Stefansson, S. L. Santangelo, J. F. Gusella, P. Sklar, B. L. Wu, M. J. Daly, Autism Consortium, Association between microdeletion and microduplication at 16p11.2 and autism. *N. Engl. J. Med.* **358**, 667–675 (2008).

12. A. M. Persico, R. Sacco, Endophenotypes in autism spectrum disorders. In: Patel V., Preedy V., Martin C., Eds. Comprehensive Guide to Autism. (Springer, 2014), pp. 77–95.

13. S. Haar, S. Berman, M. Behrmann, I. Dinstein, Anatomical abnormalities in autism?. *Cereb. Cortex* **26**, 1440–1452 (2016).

14. M. V. Lombardo, T. Pramparo, V. Gazestani, V. Warrier, R. A. I. Bethlehem, C. Carter Barnes, L. Lopez, N.E. Lewis, L. Eyler, K. Pierce, E. Courchesne, Large-scale associations between the leukocyte transcriptome and BOLD responses to speech differ in autism early language outcome subtypes. *Nat. Neurosci.* **21**, 1680–1688 (2018).

15. L. Mason, C. Moessnang, C. Chatham, L. Ham, J. Tillmann, G. Dumas, C. Ellis, C. S. Leblond, F. Cliquet, T. Bourgeron, C. Beckmann, T. Charman, B. Oakley, T. Banaschewski, A. Meyer-Lindenberg, S. Baron-Cohen, S. Bölte, J. K. Buitelaar, S. Durston, E. Loth, B. Oranje, A. Persico, F. Dell'Acqua, C. Ecker, M. H. Johnson, D. Murphy, E. J. H. Jones, Stratifying the autistic phenotype using electrophysiological indices of social perception. *Sci. Transl. Med.* **14**, eabf8987 (2022).

16. G. Horev, J. Ellegood, J. P. Lerch, Y.-E. E. Son, L. Muthuswamy, H. Vogel, A. M. Krieger, A. Buja, R. M. Henkelman, M. Wigler, A. A. Mills, Dosage-dependent phenotypes in models of 16p11.2 lesions found in autism. *Proc. Natl. Acad. Sci. U.S.A.* **108**, 17076–17081 (2011).

17. S. Martin-Brevet, B. Rodríguez-Herreros, J. A. Nielsen, C. Moreau, C. Modenato, A. M. Maillard, A. Pain, S. Richetin, A. E. Jønch, A. Y. Qureshi, N. R. Zürcher, P. Conus; 16p11.2 European Consortium; Simons Variation in Individuals Project (VIP) Consortium, W. K. Chung, E. H. Sherr, J. E. Spiro, F. Kherif, J. S. Beckmann, N. Hadjikhani, A. Reymond, R. L. Buckner, B. Draganski, S. Jacquemont, Quantifying the effects of 16p11.2 copy number variants on brain structure: A multisite genetic-first study. *Biol. Psychiatry* **84**, 253–264 (2018).

18. K. J. Friston, J. Ashburner, Generative and recognition models for neuroanatomy. *Neuroimage* **23**, 21–24 (2004).

19. S. Kundu, S. Kolouri, K. I. Erickson, A. F. Kramer, E. McAuley, G. K. Rohde, Discovery and visualization of structural biomarkers from mri using transport-based morphometry. *Neuroimage* **167**, 256–275 (2018).

20. S. Kolouri, A. B. Tosun, J. A. Ozolek, G. K. Rohde, A continuous linear optimal transport approach for pattern analysis in image datasets. *Pattern Recognit.* **51**, 453–462 (2016).

21. W. Wang, D. Slepcev, S. Basu, J. A. Ozolek, G. K. Rohde, A linear optimal transportation framework for quantifying and visualizing variations in sets of images. *Int. J. Comput. Vis.* **101**, 254–269 (2013).

22. S. Kundu, H. Huang, K. I. Erickson, E. McAuley, A. F. Kramer, G. K. Rohde, Investigating impact of cardiorespiratory fitness in reducing brain tissue loss caused by ageing. *Brain Commun.* **3**, fcab228 (2021).

23. J. A. Ozolek, A. B. Tosun, W. Wang, C. Chen, S. Kolouri, S. Basu, H. Huang, G. K. Rohde, Accurate diagnosis of thyroid follicular lesions from nuclear morphology using supervised learning. *Med. Image Anal.* **18**, 772–780 (2014).

24. S. Basu, S. Kolouri, G. K. Rohde, Detecting and visualizing cell phenotype differences from microscopy images using transport-based morphometry. *Proc. Natl. Acad. Sci. U.S.A.* **111**, 3448–3453 (2014).

25. S. Kundu, Ai in medicine must be explainable. *Nat. Med.* **27**, 1328–1328 (2021).

26. Y. Brenier, Polar factorization and monotone rearrangement of vector-valued functions. *Commun. Pure Appl. Math.* **44**, 375–417 (1991).

27. C. Villani, *Optimal Transport: Old and New* (Springer, 2008).

28. S. Kundu, A. Ghodadra, S. Fakhran, L. Alhilali, G. Rohde, Assessing postconcussive reaction time using transport-based morphometry of diffusion tensor images. *Am. J. Neuroradiol.* **40**, 1117–1123 (2019).

29. S. Kundu, B. G. Ashinsky, M. Bouhrara, E. B. Dam, S. Demehri, M. Shifat-E-Rabbi, R. G. Spencer, K. L. Urish, G. K. Rohde, Enabling early detection of osteoarthritis from presymptomatic cartilage texture maps via transport-based learning. *Proc. Natl. Acad. Sci. U.S.A.* **117**, 24709–24719 (2020).

30. W. Wang, Y. Mo, J. A. Ozolek, G. K. Rohde, Penalized fisher discriminant analysis and its application to image-based morphometry. *Pattern Recogn. Lett.* **32**, 2128–2135 (2011).

31. M. L. McHugh, Interrater reliability: The kappa statistic. *Biochem. Med.* **22**, 276–282 (2012).

32. Harvard-Oxford atlas.

33. D. Krishna B, L. Mary, A. George, Automatic Severity Evaluation of Articulation Disorder in Speech using Dynamic Time Warping. *2021 Fourth International Conference on Microelectronics, Signals & Systems (ICMSS)*, Kollam, India, (IEEE, 2021), pp. 1–6.

34. B. Rein, Z. Yan, 16p11.2 copy number variations and neurodevelopmental disorders. *Trends Neurosci.* **43**, 886–901 (2020).

35. E. Shishido, B. Aleksic, N. Ozaki, Copy-number variation in the pathogenesis of autism spectrum disorder. *Psychiatry Clin. Neurosci.* **68**, 85–95 (2014).

36. S. Neubauer, J.-J. Hublin, P. Gunz, The evolution of modern human brain shape. *Sci. Adv.* **4**, eaao5961 (2018).

37. J. P. Owen, Y. S. Chang, N. J. Pojman, P. Bukshpun, M. L. Wakahiro, E. J. Marco, J. I. Berman, J. E. Spiro, W. K. Chung, R. L. Buckner, T. P. Roberts, S. S. Nagarajan, E. H. Sherr, P. Mukherjee; Simons VIP Consortium, Aberrant white matter microstructure in children with 16p11.2 deletions. *J. Neurosci.* **34**, 6214–6223 (2014).

38. Y. S. Chang, J. P. Owen, N. J. Pojman, T. Thieu, P. Bukshpun, M. L. Wakahiro, E. J. Marco, J. I. Berman, J. E. Spiro, W. K. Chung, R. L. Buckner, T. P. L. Roberts, S. S. Nagarajan, E. H. Sherr, P. Mukherjee, Reciprocal white matter alterations due to 16p11.2 chromosomal deletions versus duplications. *Hum. Brain Mapp.* **37**, 2833–2848 (2016).

39. K. Blackmon, T. Thesen, S. Green, E. Ben-Avi, X. Wang, B. Fuchs, R. Kuzniecky, O. Devinsky, Focal cortical anomalies and language impairment in 16p11.2 deletion and duplication syndrome. *Cereb. Cortex* **28**, 2422–2430 (2018).

40. M. Sundberg, H. Pinson, R. S. Smith, K. D. Winden, P. Venugopal, D. J. Tai, J. F. Gusella, M. E. Talkowski, C. A. Walsh, M. Tegmark, M. Sahin, 16p11.2 deletion is associated with hyperactivation of human ipsc-derived dopaminergic neuron networks and is rescued by rhoa inhibition in vitro. *Nat. Commun.* **12**, 2897 (2021).

41. J. Li, T. Brickler, A. Banuelos, K. Marjon, A. Shcherbina, S. Banerjee, J. Bian, C. Narayanan, I. L. Weissman, S. Chetty, Overexpression of cd47 is associated with brain overgrowth and 16p11.2 deletion syndrome, *Proc. Natl. Acad. Sci. U.S.A.* **118**, e2005483118 (2021).

42. M. S. Jimenez-Romero, M. Fernandez-Urquiza, A. Benıtez-Burraco, Language and communication deficits in chromosome 16p11.2 deletion syndrome. *J. Speech Lang. Hear. Res.* **65**, 4724–4740 (2022).

43. K. Irie, M. Doi, N. Usui, S. Shimada, Evolution of the human brain can help determine pathophysiology of neurodevelopmental disorders, *Front. Neurosci.* **16**, 871979 (2022).

44. K. Zhang, T. J. Sejnowski, A universal scaling law between gray matter and white matter of cerebral cortex. *Proc. Natl. Acad. Sci. U.S.A.* **97**, 5621–5626 (2000).

45. J. Reber, K. Hwang, M. Bowren, J. Bruss, P. Mukherjee, D. Tranel, A. D. Boes, Cognitive impairment after focal brain lesions is better predicted by damage to structural than functional network hubs. *Proc. Natl. Acad. Sci. U.S.A.* **118**, e2018784118 (2021).

46. J. Ju, X. Yang, J. Jiang, D. Wang, Y. Zhang, X. Zhao, X. Fang, H. Liao, L. Zheng, S. Li, S.-T. Hou, L. Liang, Y. Pan, H. Li, N. Li, Structural and lipidomic alterations of striatal myelin in 16p11.2 deletion mouse model of autism spectrum disorder. *Front. Cell. Neurosci.* **15**, 718720 (2021).

47. C. Modenato, S. Martin-Brevet, C. A. Moreau, B. Rodriguez-Herreros, K. Kumar, B. Draganski, I. E. Sønderby, S. Jacquemont, Lessons learned from neuroimaging studies of copy number variants: A systematic review. *Biol. Psychiatry* **90**, 596–610 (2021).

48. Simons Vip Consortium, Simons variation in individuals project (Simons VIP): A genetics first approach to studying autism spectrum and related neurodevelopmental disorders. *Neuron* **73**, 1063–1067 (2012).

49. I. E. Sønderby, C. R. K. Ching, S. I. Thomopoulos, D. van der Meer, D. Sun, J. E. Villalon-Reina, I. Agartz, K. Amunts, C. Arango, N. J. Armstrong, R. Ayesa-Arriola, G. Bakker, A. S. Bassett, D. I. Boomsma, R. Bülow, N. J. Butcher, V. D. Calhoun, S. Caspers, E. W. C. Chow, S. Cichon, S. Ciufolini, M. C. Craig, B. Crespo-Facorro, A. C. Cunningham, A. M. Dale, P. Dazzan, G. I. de

Zubicaray, S. Djurovic, J. L. Doherty, G. Donohoe, B. Draganski, C. A. Durdle, S. Ehrlich, B. S. Emanuel, T. Espeseth, S. E. Fisher, T. Ge, D. C. Glahn, H. J. Grabe, R. E. Gur, B. A. Gutman, J. Haavik, A. K. Håberg, L. A. Hansen, R. Hashimoto, D. P. Hibar, A. J. Holmes, J.-J. Hottenga, H. E. Hulshoff Pol, M. Jalbrzikowski, E. E. M. Knowles, L. Kushan, D. E. J. Linden, J. Liu, A. J. Lundervold, S. Martin-Brevet, K. Martínez, K. A. Mather, S. R. Mathias, D. M. Mc Donald-Mc Ginn, A. F. Mc Rae, S. E. Medland, T. Moberget, C. Modenato, J. M. Sánchez, C. A. Moreau, T. W. Mühleisen, T. Paus, Z. Pausova, C. Prieto, A. Ragothaman, C. S. Reinbold, T. R. Marques, G. M. Repetto, A. Reymond, D. R. Roalf, B. Rodriguez-Herreros, J. J. Rucker, P. S. Sachdev, J. E. Schmitt, P. R. Schofield, A. I. Silva, H. Stefansson, D. J. Stein, C. K. Tamnes, D. Tordesillas-Gutiérrez, M. O. Ulfarsson, A. Vajdi, D. v'ant Ent, M. B. M. van den Bree, E. Vassos, J. Vázquez-Bourgon, F. Vila-Rodriguez, G. B. Walters, W. Wen, L. T. Westlye, K. Wittfeld, E. H. Zackai, K. Stefánsson, S. Jacquemont, P. M. Thompson, C. E. Bearden; ENIGMA-CNV Working Group; ENIGMA 22q11.2 Deletion Syndrome Working Group, Effects of copy number variations on brain structure and risk for psychiatric illness: Large-scale studies from the enigma working groups on cnvs. *Hum. Brain Mapp.* **43**, 300–328 (2022).

50. C. A. Moreau, C. R. Ching, K. Kumar, S. Jacquemont, C. E. Bearden, Structural and functional brain alterations revealed by neuroimaging in cnv carriers. *Curr. Opin. Genet. Dev.* **68**, 88–98 (2021).

51. J. P. Owen, P. Bukshpun, N. Pojman, T. Thieu, Q. Chen, J. Lee, D. D'Angelo, O. A. Glenn, J. V. Hunter, J. I. Berman, T. P. Roberts, R. Buckner, S. S. Nagarajan, P. Mukherjee, E. H. Sherr, Brain MR imaging findings and associated outcomes in carriers of the reciprocal copy number variation at 16p11.2 *Radiology* **286**, 217–226 (2018).

52. A. Kostic, J. D. Buxbaum, The promise of precision medicine in autism. *Neuron* **109**, 2212–2215 (2021).

53. American Psychiatric Association, *DSM-IV-Tr*: *Diagnostic and Statistical Manual of Mental Disorders, Text Revision* (American Psychiatric Association, 75, 2000), pp. 78–85.

54. E. Mullen, *Mullen Scales of Early Learning, AGS Edition: Manual and Item Administrative Books*, (American Guidance Services Inc., 1995) pp. 1–92.

55. C. D. Elliott, J. D. Salerno, R. Dumont, J. O. Willis, *The Differential Ability Scales - Second Edition.* D. P. Flanagan & E. M. McDonough, Eds., Contemporary intellectual assessment: Theories, tests and issues (4th ed., 2007), pp. 360–382.

56. D. Wechsler, *WAIS-administration and scoring manual.* The Psychological Corporation. (1997).

57. A. Maillard, A. Ruef, F. Pizzagalli, E. Migliavacca, L. Hippolyte, S. Adaszewski, J. Dukart, C. Ferrari, P. Conus, K. Mannik, M. Zazhytska, V. Siffredi, P. Maeder, Z. Kutalik, F. Kherif, N. Hadjikhani, J S Beckmann, A. Reymond, B. Draganski, S. Jacquemont; 16p11.2 European Consortium The 16p11.2 locus modulates brain structures common to autism, schizophrenia and obesity. *Mol. Psychiatry* **20**, 140–147 (2015).

58. J. Ashburner, C. Hutton, R. Frackowiak, I. Johnsrude, C. Price, K. Friston, Identifying global anatomical differences: Deformation-based morphometry. *Hum. Brain Mapp.* **6**, 348–357 (1998).

59. J. Ashburner, K. J. Friston, Voxel-based morphometry—The methods, *Neuroimage* **11**, 805–821 (2000).

60. J. Ashburner, C. Good, K. J. Friston, Tensor based morphometry. *Neuroimage* **11**, S465 (2000).

61. S. R. Park, S. Kolouri, S. Kundu, G. K. Rohde, The cumulative distribution transform and linear pattern classification. *Appl. Comput. Harmon. Anal.* **45**, 616–641 (2018).

62. H. Hoffmann, Violin plot (https://www.mathworks.com/matlabcentral/fileexchange/45134-violin-plot), MATLAB Central File Exchange. Retrieved May 23, 2024. (2015).

63. M. F. Beg, M. I. Miller, A. Trouve, L. Younes, Computing large deformation metric mappings via geodesic flows of diffeomorphisms. *Int. J. Comput. Vis.* **61**, 139–157 (2005).

64. A. M. Dale, B. Fischl, M. I. Sereno, Cortical surface-based analysis. *Neuroimage* **9**, 179–194 (1999).

65. T. Hastie, R. Tibshirani, J. Friedman, *The Elements of Statistical Learning: Data Mining, Inference, and Prediction. Springer Series in Statistics* (Springer, 2009).

66. H. Hotelling, *Breakthroughs in Statistics* (Springer, 1992), pp. 162–190.